Post-Print

This is the accepted version of:

A. Montero Minan, F. Scala, C. Colombo
Manoeuvre Planning Algorithm for Satellite Formations Using Mean Relative Orbital Elements
Advances in Space Research, published online 23/09/2022
doi:10.1016/j.asr.2022.09.043

The final publication is available at https://doi.org/10.1016/j.asr.2022.09.043

Manoeuvre planning algorithm for satellite formations using mean relative orbital elements

Alejandro Montero Miñan *, Francesca Scala †, Camilla Colombo‡
Politecnico di Milano, Milano, Lombardia, 20156, Italy

Formation flying missions have increased their importance thanks to the better performances that can be achieved with a distributed system of satellites. One of the most demanding challenges linked to the formation flying missions is the formulation of a robust control plan. Due to the recent developments in electrical propulsion, controllers that apply a continuous low-thrust to each spacecraft in the formation have been proposed, achieving a precise control. This idea is used in this manuscript, where an open-loop manoeuvre planning algorithm is developed, to provide the control accelerations to achieve a formation reconfiguration in a given temporal frame. The proposed algorithm is based on an innovative control technique, which relies on the mean relative orbital elements as state variables of a first-order dynamic system. It includes the effect of the gravitational field of the Earth. Finally, the algorithm is tested with two different test cases of formation flying reconfiguration, presenting and analysing their results. The test cases scenarios considered are based on possible future mission concepts in Low Earth Orbit, aiming at improving the control performances for the mission design.

I. Introduction

The importance of spacecraft formation flying has increased during recent years, mainly due to two factors. First, the possibility to use them to create novel configurations for remote sensing. In particular, the use of distributed payloads mounted on different platforms at a certain distance allows creating a virtual sensor with better capabilities with respect to the current missions for Earth observation, such as better resolution and accuracy [1]. A couple of examples of formation flying missions applied to remote sensing are the GRACE [2] and the TanDEM-X [3] missions. The other main reason why formation flying projects are becoming more popular is due to the miniaturisation of all the space-related technology, which allows using distributed payload onboard multiple small satellites to carry out a mission that would have been assigned to a big satellite a few years ago [4]. One of the advantages of satellite formation flying is the possibility to give a new dimension to Earth Observation resolution [5]. When the positions of the satellites are close to each other inside the formation, relative equations of motions are used to predict and control their position and velocity [6]. As a result, several advancements in the close-proximity operations field have been made. One of

*MSc Student, Aerospace Science & Technology Department, Via La Masa 34
†PhD Candidate, Aerospace Science & Technology Department, Via La Masa 34 (corresponding author: francesca1.scala@polimi.it)
‡Associate Professor of Orbital Mechanics, Aerospace Science & Technology Department, Via La Masa 34

the most recent advancements in the relative motion theory for Low Earth Orbits (LEO) are included in [7], where a framework for precise relative motion propagation in LEO is described, using mean Relative Orbital Elements (ROEs) as state variables. This article also includes a new approach to transform osculating orbital elements into mean orbital elements and vice-versa. These techniques contribute to the simplification of the problem, allowing taking into account only the secular effects of the perturbations in the mean orbital elements, removing the high-frequency variations due to the short term effects.

Another important aspect of formation flying is the development of onboard controllers. Historically, the controllers were formulated with cartesian-based relative motion models and with different techniques, ranging from linear quadratic regulators [8, 9] to model predictive control [10], including trajectory generation using convex optimal problems [11, 12]. In these references, the problem considers continuous control over the satellites. However, there are also examples in which the control is performed with impulsive manoeuvres. In these cases, the control profile is computed imposing the final conditions at the end of the manoeuvring period [13, 14]. On the other hand, examples of controllers based on the ROEs description for the formation flying relative motion are of particular importance for this work. Most of these controllers are conceived for impulsive control configurations and are based on the eccentricity/inclination (e/i) relative vector separation, inherited from the geostationary satellites. Some of them were employed in real missions, such as in the GRACE formation to switch the lead-follower roles [15], the TanDEM-X formation, where the controller was used to maintain one of the satellites orbiting in a tube of 250 m around the trajectory of the second one [16, 17], and the PRISMA mission, whose main objective was to test several technologies related to formation flying guidance and control [18].

Even though there exist different control designs based on ROEs for impulsive control, only a few cases consider continuous control over the satellites during the manoeuvres. This trend has started to shift recently due to the electrical propulsion development, whose higher specific impulses and efficiency in recent years [19] have allowed considering continuous thrust for fine control, such as in the Formation Flying L-Band Aperture Synthesis (FFLAS) formation [20]. One of the main limitations of electric propulsion is the small thrust output, which must be taken into account in the formulation of the problem. In [7, 21, 22], the ROEs are used to design a controller for relative motion based on low thrust technology. The authors in [7] obtain a piece-wise constant control using techniques similar to the ones used in the impulsive manoeuvres computation to impose a relative trajectory for a manoeuvre. In [21], the desired formation configuration is achieved through a continuous control formulated with the Lyapunov theory, in eulerian orbital elements. In [22], the ROEs are computed through the modification of the integration constants of the Hill-Clohessy-Wiltshire equations to avoid singularities. This work uses the Lyapunov theory to follow a desired set of ROEs.

Finally, there are some works where the controller design is based on the relative orbital set defined in [23] and on continuous control. One example is [24], in which the design of a computationally efficient strategy for a formation reconfiguration in J_2-perturbed near-circular orbits using a finite number of finite-time manoeuvre is included. Moreover,

in [25], the author controls the formation configuration through a linear quadratic regulator. Finally, in [26], the authors use a Lyapunov-based controller to reconfigure the formation, while including a reference governor that can enforce wall, thrust and time constraints and considering J_2 and differential drag effects.

Given the small number of controllers based on the ROE set defined in [23] and with continuous control, this article aims at implementing a new continuous-time model for the ROEs' dynamics based on [7], under the perturbation effects caused by the non-spherical mass distribution of the Earth. Moreover, it aims at including this model in a continuous-time and ROEs-based control algorithm: an open loop manoeuvre planning algorithm.

The manuscript is organised into different sections. Section II introduces the relative motion's dynamic model, including both the natural dynamics and the control matrix. Then, in Section III the open loop manoeuvre planning algorithm is developed using the dynamic model, both in classical and convex form. This control algorithm is tested with two different satellite formations and its performance for both cases is analysed in Section IV. Finally, Section V covers the conclusions from the results of the analysis.

II. Dynamic model

The first elements required to define a control problem are the natural temporal evolution of the state variables and the system control matrix, which maps the effects of the control variables into the state variables. This section covers the process followed to obtain both of them.

A. State variable set

As aforementioned, this article aims at developing a new continuous-time model for the relative dynamics using ROEs. However, there are several ROEs sets, therefore a clarification is due. In this article, the quasi-non singular set of orbital elements is selected to work with circular orbits without singularity problems. In particular, the ROEs considered are the relative semi-major axis δa, the relative longitude $\delta\lambda$, the relative eccentricity vector components δe_x and δe_y and the relative inclination vector components δi_x and δi_y, as described in [7].

$$\boldsymbol{\delta\alpha} = [\delta a, \delta\lambda, \delta e_x, \delta e_y, \delta i_x, \delta i_y]^T = [\Delta a/a_c, \Delta u + \Delta\Omega\cos(i_c), \Delta e_x, \Delta e_y, \Delta i, \Delta\Omega\sin(i_c)]^T \tag{1}$$

Where Δ is the difference between the deputy's orbital element and the chief's one, a is the semi-major axis, $u = \omega + \theta$ is the argument of latitude, ω is the argument of perigee, θ the true anomaly, e_x and e_y are the eccentricity vector components, i is the orbit inclination, Ω is the right ascension of the ascending node and the subscript $\cdot_c$ indicates that the orbital element belongs to the chief. The relative inclination vector has a modulus equal to the sine of the difference between the two satellites' inclinations and is co-planar to the chief's orbital plane. It points towards the relative ascending node, which is the point of the chief's orbit at which the deputy crosses the orbital plane in the same

direction as the chief's angular momentum. The relative inclination vector expression can be simplified down to the one shown in Eq. (1) considering that the differences between the chief's and deputy's orbital planes are small ($\Delta i \ll 1$ and $\Delta\Omega \ll 1$) and applying spherical trigonometry [15]. On the other hand, the expression for the relative eccentricity vector can be obtained as the difference of the deputy's and chief's eccentricity vectors, and is suitable only if both orbital planes are close enough (same conditions as for the relative inclination vector simplification).

The ROEs can be directly related to the relative cartesian coordinates through a linear relation [23]. In particular, the transformation between ROEs and relative cartesian coordinates is necessary for the control algorithm's development. Eq. (2) shows the linear relation between the ROEs and the relative cartesian coordinates:

$$\begin{bmatrix} X \\ Y \\ Z \\ v_X \\ v_Y \\ v_Z \end{bmatrix} = \begin{bmatrix} a_c & 0 & -a_c\cos(u) & -a_c\sin(u) & 0 & 0 \\ 0 & a_c & 2a_c\sin(u) & -2a_c\cos(u) & 0 & 0 \\ 0 & 0 & 0 & 0 & a_c\sin(u) & -a_c\cos(u) \\ 0 & 0 & a_c n\sin(u) & -a_c n\cos(u) & 0 & 0 \\ -\frac{3}{2}na_c & 0 & 2a_c n\cos(u) & 2a_c n\sin(u) & 0 & 0 \\ 0 & 0 & 0 & 0 & a_c n\cos(u) & a_c n\sin(u) \end{bmatrix} \begin{bmatrix} \delta a \\ \delta\lambda \\ \delta e_x \\ \delta e_y \\ \delta i_x \\ \delta i_y \end{bmatrix} \tag{2}$$

In Eq. (2), the variables X, Y, and Z represent the relative position of the deputy with respect to the chief in the Radial-Transversal-Normal (RTN) frame fixed to the chief, v_i are instead the deputy's relative velocities in this same frame and n represents the chief's angular velocity $n = \sqrt{\frac{\mu}{a_c^3}}$. These six variables are collected into a cartesian state vector denoted as $\boldsymbol{x}$. This linear relation's independent variable is the chief's angular position along its orbit, described by its argument of latitude u.

The linear transformation reported in Eq. (2) is obtained from [23] and is defined for Keplerian motion. The problem formulation at hand considers also the effects of the J_2 perturbation, but this linear transformation is also valid when considering the J_2 perturbation during long periods, obtaining a completely bounded error for satellite distances up to 1 km [23].

B. Natural relative dynamics' model

Once the state variables have been introduced and their relation to the cartesian coordinates shown, it is possible to present the dynamic model. In this manuscript, we considered a model based on the work presented in [7], where an analytical framework for precise relative motion in LEO is developed. It describes how to convert the osculating ROEs into mean ones and vice-versa, and presents the natural dynamics in the mean orbital elements in a perturbed environment.

The transformation from osculating to mean orbital elements is introduced because working with the osculating

set of orbital elements is more computationally expensive due to their short-term periodic variations. Working with their mean counterpart has the advantage of neglecting these variations, resulting in a smoother control [27]. This transformation is necessary because the position and velocity measurements obtained for each spacecraft during operation give information only about their instantaneous state, and therefore, only about the osculating orbital elements.

The dynamics are expressed using a state transition matrix (STM) based on ROEs, which also includes the geopotential perturbation effects [7]. The expression for the STM is reported in Eq. (3), where the orbital elements are referred to the mean elements of the chief, and the subscript $\cdot_0$ refers to the initial condition at t_0.

$$\Phi(\boldsymbol{\alpha_0}, \Delta t) = \begin{bmatrix} 1 & 0 & 0 & 0 & 0 & 0 \\ a\Delta t \sum_p g_a^{(p)} & 1 & \Delta t \sum_p g_{e_x}^{(p)} & \Delta t \sum_p g_{e_y}^{(p)} & \Delta t \sum_p g_i^{(p)} & 0 \\ a\Delta t A_1 \sum_p \dot{\omega}_a^{(p)} & 0 & C + \Delta t A_1 \sum_p \dot{\omega}_{e_x}^{(p)} & -S + \Delta t A_1 \sum_p \dot{\omega}_{e_y}^{(p)} & \Delta t A_1 \sum_p \dot{\omega}_i^{(p)} & 0 \\ a\Delta t A_2 \sum_p \dot{\omega}_a^{(p)} & 0 & S + \Delta t A_2 \sum_p \dot{\omega}_{e_x}^{(p)} & C + \Delta t A_2 \sum_p \dot{\omega}_{e_y}^{(p)} & \Delta t A_2 \sum_p \dot{\omega}_i^{(p)} & 0 \\ 0 & 0 & 0 & 0 & 1 & 0 \\ a \sin(i) \Delta t \sum_p \dot{\Omega}_a^{(p)} & 0 & \sin(i) \Delta t \sum_p \dot{\Omega}_{e_x}^{(p)} & \sin(i) \Delta t \sum_p \dot{\Omega}_{e_y}^{(p)} & \sin(i) \Delta t \sum_p \dot{\Omega}_i^{(p)} & 1 \end{bmatrix} \tag{3}$$

Where, $\sum_p$ represents a summation for varying p, which is the index of the ordered set of the considered zonal harmonics ($\{J_0, J_2, J_2^2, J_4, J_6\}$) and the subscript notation $f_x^{(p)}$ is used to denote the partial derivatives of $f^{(p)}$ (generated by the J_p contribution) with respect to the element x. The notation J_0 was used for the Keplerian motion, where only $\dot{M} = n$. The expressions for S, C, A_1, A_2, and g are included in Eq. (4).

$$\begin{aligned} &S = \sin\left(\textstyle\sum_p \dot{\omega}^{(p)} \Delta t\right) \quad C = \cos\left(\textstyle\sum_p \dot{\omega}^{(p)} \Delta t\right) \\ &A_1 = -(Se_{x0} + Ce_{y0}) \quad A_2 = (Ce_{x0} - Se_{y0}) \\ &g = \dot{\omega} + \dot{M} + \dot{\Omega}\cos(i) \end{aligned} \tag{4}$$

Where e_{x0} and e_{y0} are the eccentricity vector components at the reference instant t_0, $\dot{\omega}$ the argument of perigee's temporal variation rate, $\dot{\Omega}$ is the right ascension of the ascending node temporal variation rate and $\dot{M}$ is the angular velocity associated to the mean anomaly. It is worth noting that the temporal evolution obtained with the STM is general from the Earth's mass distribution point of view, meaning that it is valid whichever gravity potential order is considered. As a consequence, the accuracy provided by this model can be tuned and adapted to the needs of different missions. Also, the model is valid for a generic eccentric orbit, not limited to circular or quasi-circular ones. With this state transition matrix, it is possible to obtain the ROEs of the deputy at $t = t_0 + \Delta t$ if their values and the chief's orbital

elements at $t = t_0$ are known:

$$\boldsymbol{\delta\alpha}(t_0 + \Delta t) = \Phi(\boldsymbol{\alpha_0}, \Delta t) \cdot \boldsymbol{\delta\alpha}_0 \tag{5}$$

Even though this expression can be used to compute the values of the ROEs at a generic time instant, a continuous expression for the system dynamics is required to formulate the control problems.

To obtain a continuous, closed-form expression for the time derivatives of the ROEs, the process followed by [28] is used, however in the opposite direction. In this reference, the authors use the continuous, closed-form expressions of the time derivatives to obtain state transition matrices for different models. The objective of this article, is to obtain the time derivatives from the STM, and the process followed is described below.

- The deputy's orbital elements $\boldsymbol{\alpha_d}(t)$ are expressed explicitly as a function of the chief's ones $\boldsymbol{\alpha_c}(t)$ and the ROEs $\boldsymbol{\delta\alpha}(t)$.
- The temporal evolution of the ROEs can be then expressed only as a function of those two variables and other relevant parameters γ (such as solar radiation pressure, the harmonics coefficients...): $\boldsymbol{\delta\dot{\alpha}} = \vec{f}(\boldsymbol{\alpha_d}(\boldsymbol{\alpha_c}(t), \boldsymbol{\delta\alpha}(t)), \boldsymbol{\alpha_c}(t), \gamma)$.
- Since the aim is to obtain an easily solvable linear system, the non-linear dependence with the state (the ROEs) must be eliminated. A first-order Taylor expansion centred around $\boldsymbol{\delta\alpha} = 0$ can be done, as shown in Eq. (6). Here, the matrix A was obtained with a chain rule derivative. The constant term of the Taylor expansion around $\boldsymbol{\delta\alpha} = 0$ must be zero, since the temporal evolution of the ROEs must be zero if both satellites have the exact same orbital elements.

$$\begin{aligned} \boldsymbol{\delta\dot{\alpha}} &= A(\boldsymbol{\alpha}_c(t), \gamma)\boldsymbol{\delta\alpha}(t) + O(\delta\alpha^2) \\ A(\boldsymbol{\alpha}_c(t), \gamma) &= \frac{\partial \delta\dot{\alpha}}{\partial \alpha_d}\Big|_{\delta\alpha=0} \frac{\partial \alpha_d}{\partial \delta\alpha}\Big|_{\alpha_d=\alpha_c} \end{aligned} \tag{6}$$

- Once the temporal derivative has been approximated as a linear function of the state, a Taylor expansion of the state at time $t = t_0 + \Delta t$ can be done: $\boldsymbol{\delta\alpha}(t_0+\Delta t) \approx \boldsymbol{\delta\alpha_0} + \boldsymbol{\delta\dot{\alpha}}|_{t_0}\Delta t$. This implies that deriving $\boldsymbol{\delta\alpha}(t_0+\Delta t) = \Phi(\alpha_{c,0}, \Delta t)\boldsymbol{\delta\alpha_0}$ with respect to Δt should yield an expression for $\boldsymbol{\delta\dot{\alpha}}$ at $t = t_0$ and with an expression similar to that in Eq. (6).

By deriving the state transition matrix expression in Eq. (3) with respect to the temporal variable Δt, the expression obtained for the perturbed dynamics in ROEs is:

$$\boldsymbol{\delta\dot{\alpha}}_k \approx \begin{bmatrix} 0 & 0 & 0 & 0 & 0 & 0 \\ a\sum_p g_a^{(p)} & 0 & \sum_p g_{e_x}^{(p)} & \sum_p g_{e_y}^{(p)} & \sum_p g_i^{(p)} & 0 \\ aA_1\sum_p \dot{\omega}_a^{(p)} & 0 & -SK^* + A_1\sum_p \dot{\omega}_{e_x}^{(p)} & -CK^* + A_1\sum_p \dot{\omega}_{e_y}^{(p)} & A_1\sum_p \dot{\omega}_i^{(p)} & 0 \\ aA_2\sum_p \dot{\omega}_a^{(p)} & 0 & CK^* + A_2\sum_p \dot{\omega}_{e_x}^{(p)} & -SK^* + A_2\sum_p \dot{\omega}_{e_y}^{(p)} & A_2\sum_p \dot{\omega}_i^{(p)} & 0 \\ 0 & 0 & 0 & 0 & 0 & 0 \\ a\sin(i)\sum_p \dot{\Omega}_a^{(p)} & 0 & \sin(i)\sum_p \dot{\Omega}_{e_x}^{(p)} & \sin(i)\sum_p \dot{\Omega}_{e_y}^{(p)} & \sin(i)\sum_p \dot{\Omega}_i^{(p)} & 0 \end{bmatrix} \boldsymbol{\delta\alpha}_k \tag{7}$$

The expressions in Eq. (7) are the same as in Eq. (3), except for the new term K^*, which corresponds to the derivative with respect to Δt of the arguments inside the trigonometric functions S and C. In Eq. (7), the subscript $\cdot_k$ is included to remark the fact that this approximation is only valid for a certain time instant t_k. To obtain the desired $\boldsymbol{\delta\dot{\alpha}_k}$ for each t_k, the ROEs' values at that same time instant are required. The plant matrix A in Eq. (7) has the same properties as the transition matrix in Eq. (3): it is valid for any order of the Earth's gravity potential and it is not limited to circular or quasi-circular orbits, making it a versatile tool. In this article the main effects of the first zonal harmonic J_2 are considered to formulate the control problems, since this provides the major contribution in LEO orbits. For this reason, in the plant matrix A in Eq. (7) the variable p is substituted by $p = 2$. The expression of the plant matrix A formulated to consider only the J_2 effect is shown in Eqs. (8) and (9) [7].

$$A = \begin{bmatrix} 0 & 0 & 0 & 0 & 0 & 0 \\ A_{2,1} & 0 & A_{2,3} & A_{2,4} & A_{2,5} & 0 \\ A_{3,1} & 0 & A_{3,3} & A_{3,4} & A_{3,5} & 0 \\ A_{4,1} & 0 & A_{4,3} & A_{4,4} & A_{4,5} & 0 \\ 0 & 0 & 0 & 0 & 0 & 0 \\ A_{6,1} & 0 & A_{6,3} & A_{6,4} & A_{6,5} & 0 \end{bmatrix} \tag{8}$$

$$
\begin{aligned}
A_{2,1} &= -\tfrac{3}{2}n - \tfrac{21}{8}K_2 nH(\eta+1)/\eta^4 & A_{3,1} &= -\tfrac{21}{8}K_2 nA_1 K/\eta^4 \\
A_{2,3} &= \tfrac{3}{4}K_2 e_x nH(3\eta+4)/\eta^6 & A_{3,3} &= -S\tfrac{3}{4}K_2 nK/\eta^4 + 3K_2 ne_x A_1 K/\eta^6 \\
A_{2,4} &= \tfrac{3}{4}K_2 e_y nH(3\eta+4)/\eta^6 & A_{3,4} &= -C\tfrac{3}{4}K_2 nK/\eta^4 + 3K_2 ne_y A_1 K/\eta^6 \\
A_{2,5} &= -\tfrac{3}{4}K_2 n\sin(2i)(3\eta+4)/\eta^4 & A_{3,5} &= -\tfrac{15}{4}K_2 nA_1 \sin(2i)/\eta^4 \\
A_{4,1} &= -\tfrac{21}{8}K_2 nA_2 K/\eta^4 & A_{6,1} &= \tfrac{21}{8}K_2 n\sin(2i)/\eta^4 \\
A_{4,3} &= C\tfrac{3}{4}K_2 nK/\eta^4 + 3K_2 ne_x A_2 K/\eta^6 & A_{6,3} &= -3K_2 e_x n\sin(2i)/\eta^6 \\
A_{4,4} &= -S\tfrac{3}{4}K_2 nK/\eta^4 + 3K_2 ne_y A_2 K/\eta^6 & A_{6,4} &= -3K_2 e_y n\sin(2i)/\eta^6 \\
A_{4,5} &= -\tfrac{15}{4}K_2 nA_2 \sin(2i)/\eta^4 & A_{6,5} &= \tfrac{3}{2}K_2 n\sin^2(i)/\eta^4
\end{aligned}
\tag{9}
$$

In these equations, n corresponds to the chief's angular velocity, i is the chief's inclination, $\eta = \sqrt{1-e^2}$, where e is the chief's eccentricity, and $e_x = e\cos(\omega)$ and $e_y = e\sin(\omega)$ are the chief's eccentricity vector components. The chief's mean semi-major axis, inclination and eccentricity are constants for the considered formulation since they are not affected by the secular effect. However, that is not true for the argument of perigee, whose variation produces a change in the eccentricity vector components. The argument of perigee and eccentricity vector components' temporal evolutions are needed to evaluate the state vector's derivatives at different time instants. Considering only the J_2 effect, the following temporal evolutions are considered [7]:

$$
e_x(t) = e_{x0}\cos(\dot{\omega}(t-t_0)) - e_{y0}\sin(\dot{\omega}(t-t_0)) \tag{10}
$$

$$
e_y(t) = e_{x0}\sin(\dot{\omega}(t-t_0)) + e_{y0}\cos(\dot{\omega}(t-t_0)) \tag{11}
$$

$$
\dot{\omega} = \frac{3}{4}J_2\left(\frac{R_\oplus}{a(1-e^2)}\right)^2 n(5\cos^2(i)-1) \tag{12}
$$

In Eqs. (10) to (12) $\dot{\omega}$ represents the argument of perigee's temporal variation rate and $R_\oplus$ is the equatorial Earth's radius. On the other hand, the expressions for the parameters appearing in Eq. (9) are:

$$
\begin{aligned}
K_2 &= J_2(R_\oplus/a)^2 \\
K &= 5\cos^2(i)-1 & H &= 3\cos^2(i)-1 \\
S &= \sin(\tfrac{3}{4}K_2 n\Delta t K/\eta^4) & C &= \cos(\tfrac{3}{4}K_2 n\Delta t K/\eta^4) \\
A_1 &= -(Se_x + Ce_y) & A_2 &= (Ce_x - Se_y)
\end{aligned}
\tag{13}
$$

Where e_x and e_y correspond to the values in in Eqs. (10) and (11), evaluated at the time instant for which the derivative is being computed. It is worth commenting the fact that there is a Δt term inside the expressions of S and C. In the discrete formulation of the problem $\delta\alpha(t_0+\Delta t) \approx \delta\alpha_0 + \delta\dot{\alpha}|_{t_0}\Delta t$, this Δt represents the time step between

two successive time instants. For a totally continuous formulation, the temporal distance between two successive state evaluations tends to zero ($\Delta t \longrightarrow 0$) and therefore $C \longrightarrow 1$ and $S \longrightarrow 0$. However, considering how this continuous model was obtained from a discrete formulation and the fact that it is going to be used in a numerical integration scheme (which are intrinsically discrete), the term Δt is kept, representing now the numerical integration time step. For a small enough integration step, the term C is close to 1, while the term S remains close to 0.

The state variables' temporal evolution obtained with this model has been validated using GMAT v.R2020a in order to validate the precision, including only the J_2 effects [29]. It is used to propagate two different satellites independently, deriving the temporal evolution of the osculating ROEs. The initial condition for the simulation is reported in Tables 1 and 2.

Table 1 Mean orbital elements sets for the chief and the deputy

	a [m]	**e** [-]	**i** [º]	**Ω** [º]	ω [º]	M_0 [º]
Chief	6868136.3	0.001	98.2	9	60	-60
Deputy	6868136.3	$9.928 \cdot 10^{-4}$	98.2004	9.0007	59.2723	-59.2722

Table 2 Relative orbital elements

$a_c\delta a$ [m]	$a_c\delta\lambda$ [m]	$a_c\delta e_x$ [m]	$a_c\delta e_y$ [m]	$a_c\delta i_x$ [m]	$a_c\delta i_y$ [m]
0	0	50	-86.6	50	86.6

The ROEs were defined imposing $a\delta e = a\delta i = 100$ m, $\theta = 120$ º and $\psi = 60$ º. From the mean orbital elements in Table 1, the osculating ones are computed to initialise the propagation. A first order mean to osculating transformation based on Brouwer's theory is used, considering only the J_2 effect [30]. Then, a numerical propagation of the previously presented model is performed to compare the temporal evolution of both ROEs sets, the mean and the osculating ones, as shown in Fig. 1.

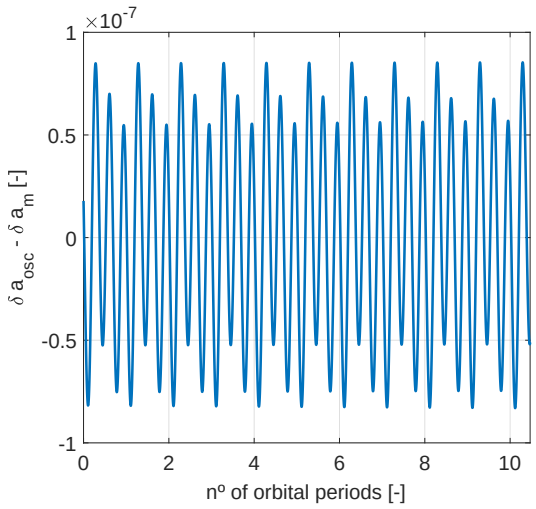

(a) Relative semi-major axis.

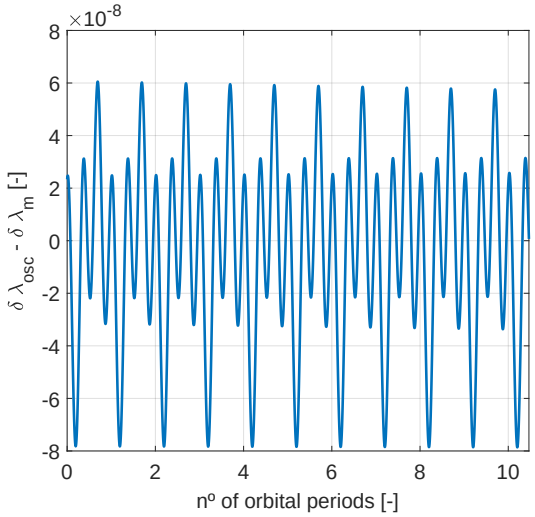

(b) Relative longitude.

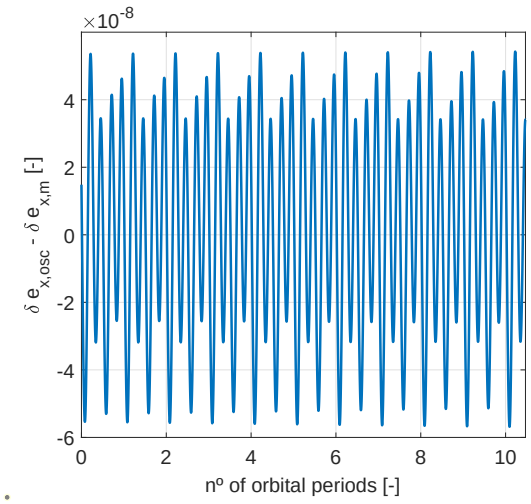

(c) Relative eccentricity vector component x.

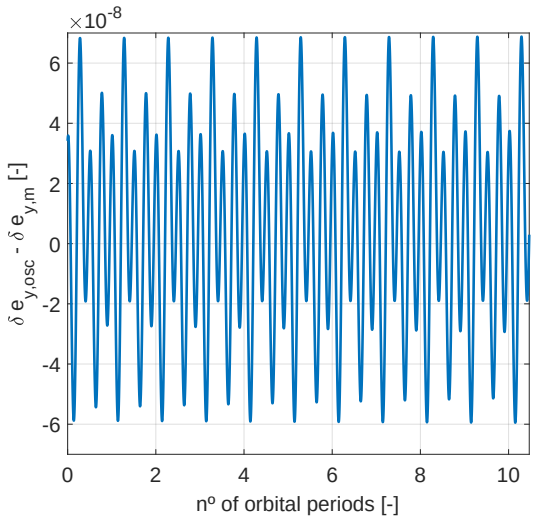

(d) Relative eccentricity vector component y.

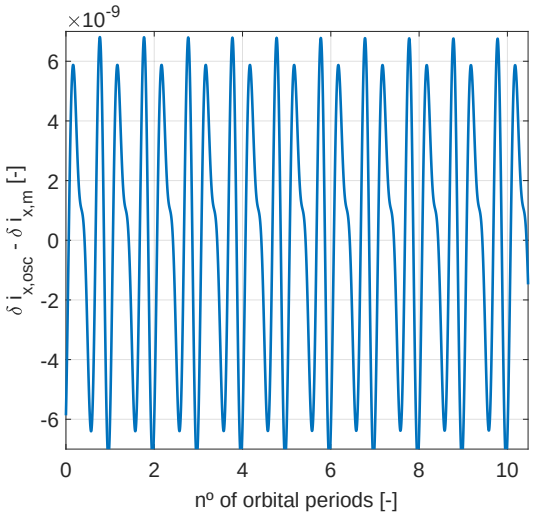

(e) Relative inclination vector component x.

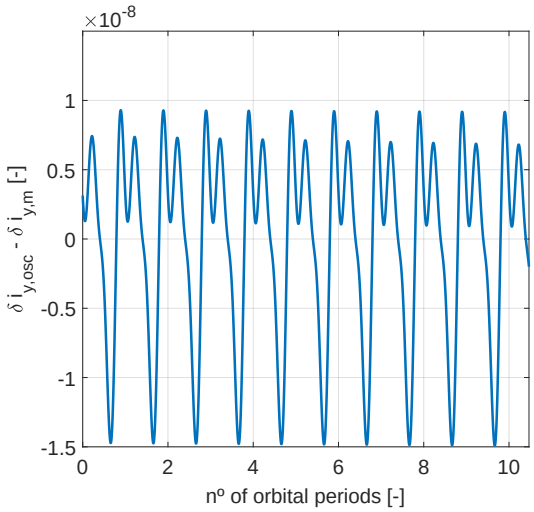

(f) Relative inclination vector component y.

Fig. 1 Difference between osculating and mean relative orbital elements.

Fig. 1 shows the differences between the osculating ROEs computed independently with GMAT and the mean ones obtained from the numerical integration of the model presented in Eq. (7), using the plant matrix A described in Eqs. (8) and (9). They are all below $1 \cdot 10^{-7}$ and periodic functions centred at 0, meaning that the mean ROEs are actually the mean values of the osculating ones. The only ROEs difference with a perceptible non-zero mean is the relative longitude. Considering that this ROE takes values in the order of $1 \cdot 10^{-7}$, which can be seen in Fig. 2, a difference in the mean of the osculating relative longitude and the modelled one in the order of $1 \cdot 10^{-9}$ can be considered negligible. These results validate the previously presented model for the ROEs' dynamics under J_2 influence.

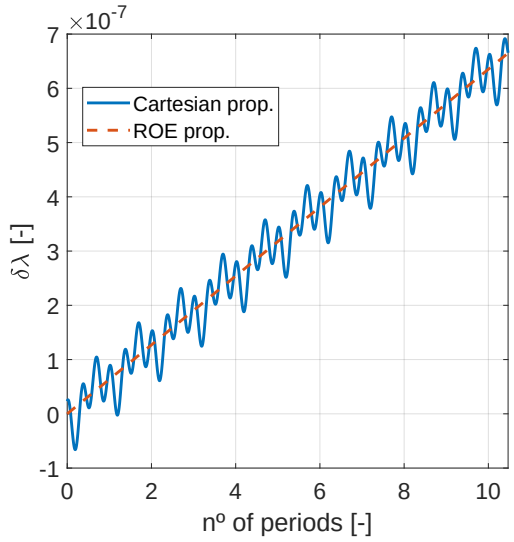

Fig. 2 Relative longitude $\delta\lambda$ temporal evolution.

C. Control matrix

Once the system's dynamic model has been obtained, the next element for the control problem's formulation is the control matrix computation. This control matrix describes how the control actions affect the state variables, the ROEs in this case. The control variables selected for these problems are three independent accelerations, described in the deputy's RTN frame. These accelerations are provided by a set of low-thrust thrusters, such as the electric ones mentioned in Section I.

To obtain this control matrix, the Gauss' Variational Equations are used. In particular, the derivation starts from the matrix in Eq. 16 from [23]. Then, deriving with respect to time the ROEs and considering that control variables act only on the deputy, which implies that the chief's orbital elements are constant, it is possible to obtain the control matrix B shown in Eq. (14). Even though the relative longitude time derivative has a term associated with the difference in the orbital periods of the chief and the deputy, this term is not related to the control accelerations, and therefore it is not included in the control matrix.

$$B = \frac{1}{n \cdot a} \begin{bmatrix} 0 & 2 & 0 \\ -2 & 0 & 0 \\ \sin(u) & 2\cos(u) & 0 \\ -\cos(u) & 2\sin(u) & 0 \\ 0 & 0 & \cos(u) \\ 0 & 0 & \sin(u) \end{bmatrix} \tag{14}$$

In Eq. (14) the term $n \cdot t$ has been substituted by the chief's mean argument of latitude u, as in [23]. Considering that the difference between the deputy's semi-major axis and the chief's one is negligible for very close formations, the angular velocity and semi-major axis values included in this expression can be taken as those of the chief. On the contrary, the term $B_{1,2}$ should include the ratio between the semi-major axis $\frac{a_d}{a_c}$ and the angular velocity and semi-major axis appearing at the denominator should be the deputy's ones. Another implicit assumption is the fact that the difference between both inclinations is negligible $\Delta i \ll 1$, which is an assumption associated to the ROEs definition in Eq. (1). This same matrix has been used in other works, such as [6, 31] and can be algebraically obtained from the control matrix used in [22].

D. Final model formulation

This section gathers the results from the previous ones and provides the final dynamic model for the system, including both the natural dynamics and the control:

$$\dot{\boldsymbol{\delta\alpha}} = A\boldsymbol{\delta\alpha} + B\boldsymbol{u} \tag{15}$$

Where $\boldsymbol{u}$ is the control variable including the three accelerations in the RTN frame.

III. Open-loop manoeuvre planning algorithm

Having introduced the relative dynamics' model, it can be used to formulate the open-loop manoeuvre planning algorithm, which is based on an optimal control problem's resolution. There are several possible ways to solve an optimal control problem. In this work, we select a control strategy based on convex optimisation [32], which has already been used for trajectory optimisation in [11, 12, 33, 34]. The transformation of the classical optimal control problem into a convex formulation ensures that the solution is unique. Moreover, thanks to the lower computational effort with respect to the classical control approaches, it could be implemented on-board the satellites, which have limited computational capabilities [12, 33]. However, convexification of the safety distance constraint (which is introduced later in this section) provides an overly conservative solution. This is solved using Sequential Convex Programming (SCP), reducing the difference between the real problem and the convex one via iterations [11].

A. Classical optimal control problem definition

The first step towards the convex optimal problem modelling is formulating the classical one, meaning, the objective function for the optimal control problem and all the equality and inequality constraint to which it is subjected. The main objective of this manoeuvre planning algorithm is to change the deputies' position in the formation, to go from a configuration A to another one B. This problem can be solved in two different ways: the first is the minimisation of the manoeuvre time with a fixed maximum ΔV, while the second one is minimisation of the fuel used to complete the manoeuvre in a fixed time interval. Following the process in [12], the problem solved is the minimisation of the fuel

used during a manoeuvre with a fixed duration. Taking this into account, the objective function for the optimal control problem is described in Eq. (16).

$$J = \sum_{j=1}^{j=N} \int_{t_0}^{t_f} ||\boldsymbol{u_j(t)}||_1 dt \tag{16}$$

Where the subindex $\cdot_j$ refers to a certain deputy, being N the total number of deputies in the formation, and $||\boldsymbol{u_j(t)}||_1$ is the 1-norm of the control action for deputy j. This objective function computes the control action's integral over the manoeuvre duration and then sums it up for all deputies, meaning that this function minimises the total ΔV considering all deputies, and since the total ΔV budget is directly related to the fuel consumption, this is equivalent to minimising this same fuel used.

Once the objective function is defined, the next step is the definition of the problem's constraints. The first one that needs to be considered is the system's dynamics, described by Eq. (15). First order linear dynamics is a requirement for the later convexification of the problem, with which Eq. (15) is compliant. Even though all the terms in Eq. (15) are time dependant, the (t) notation has been dropped for readability's sake. A second set of constraints that should be considered is the initial and final conditions of the state variables.

$$\begin{cases} \boldsymbol{\delta\alpha_j}(t_0) = \boldsymbol{\delta\alpha_{j,0}} \\ \boldsymbol{\delta\alpha_j}(t_f) = \boldsymbol{\delta\alpha_{j,f}} \end{cases} \tag{17}$$

Where the subindex $\cdot_0$ corresponds to the initial conditions and $\cdot_f$ to the final ones. Usually, the initial and final configurations are described by relative cartesian positions with respect to the chief, not in terms of the ROEs. This means that to obtain the initial and final conditions for the state variables, these cartesian coordinates have to be transformed into ROEs. This is performed inverting the linear relation described in Eq. (2), setting X, Y and Z as the initial/final positions in the formation and the relative velocities all equal to zero, while taking into account that $u = n \cdot t$.

This algorithm is developed for continuous thrust manoeuvres, which are usually limited in terms of thrust level available. This poses a limit in the control action available for the deputies.

$$||\boldsymbol{u_j}(t)||_1 \leq a_{max,j} \tag{18}$$

Where $a_{max,j}$ is the maximum available thrust for deputy j. These limits may be different in each direction for the same spacecraft, but this situation is considered during the problem's discretisation.

The last of the constraints considered is the inter-satellite distance constraint. This is key to ensure the formation's safety during the manoeuvres. In the control problem, the deputies are considered point masses for Eq. (15), however this assumption cannot be used for this constraint's formulation. The actual deputies' diameter should be considered,

along with a safety margin, to define this distance constraint. In [12], the state variables are the deputies' relative cartesian positions, allowing a more straightforward formulation of the safety constraint. On the other hand, the relative cartesian positions are a function of the ROEs, as in Eq. (2). Calling L_j to the first three rows of the matrix in Eq. (2), which corresponds to the relative cartesian positions, the safety distance constraint can be formulated in the ROEs space as:

$$||L_j(t)\boldsymbol{\delta\alpha_j}(t) - L_i(t)\boldsymbol{\delta\alpha_i}(t)||_2 \geq d_{th} \tag{19}$$

Where the subindex $\cdot_i$ refers to a ith deputy different from the jth one and d_{th} is the minimum inter-satellite distance allowable during the manoeuvre. Once that the objective function and all constraint have been defined, it is possible to formulate the complete optimal control problem as in Eq. (20).

$$\begin{aligned}
&\text{minimise:} && J = \textstyle\sum_{j=1}^{j=N} \int_{t_0}^{t_f} ||\boldsymbol{u_j(t)}||_1 dt \\
&\text{subject to:} && \boldsymbol{\delta\dot{\alpha}_j}(t) = A_j\boldsymbol{\delta\alpha_j} + B_j\boldsymbol{u_j} \\
& && \boldsymbol{\delta\alpha_j}(t_0) = \boldsymbol{\delta\alpha_{j,0}} \\
& && \boldsymbol{\delta\alpha_j}(t_f) = \boldsymbol{\delta\alpha_{j,f}} \\
& && ||\boldsymbol{u_j}(t)||_1 \leq a_{max,j} \\
& && ||L_j(t)\boldsymbol{\delta\alpha_j}(t) - L_i(t)\boldsymbol{\delta\alpha_i}(t)||_2 \geq d_{th}
\end{aligned} \tag{20}$$

B. Convex optimal control problem formulation

To apply the convex optimal control techniques, the problem described in Eq. (20) has to be reformulated in terms of the convex formulation requirements. Both the objective function and the inequality constraint must be convex and the equality constraints must be affine [12]. The first step to formulate the problem in convex form is discretising it and then, reformulating those equations that are not compliant with the previous requirements. The discretisation procedure followed in this article is based on the one performed in [12]. The time instants are discretised in terms of a time step Δt, forming a vector with size K, where each time instant is identified by the time index $k = 1, ..., K$. The dynamics of each jth deputy can be approximated by different discretisation techniques. However, due to its simplicity and adequate precision as long as the time step Δt is sufficiently small, the Forward Euler discretisation procedure is selected. Considering this, the dynamics of each deputy can be written as:

$$\boldsymbol{\delta\alpha_j}[k+1] = (I + A_{j,k}\Delta t)\boldsymbol{\delta\alpha_j}[k] + \Delta t B_{j,k}\boldsymbol{u}_j[k] \tag{21}$$

Where $A_{j,k}$ is the jth deputy's plant matrix, $B_{j,k}$ is its control matrix and $\boldsymbol{u}_j$[k] contains its control variables, all of them evaluated at time instant t_k. Recalling how the plant matrix A was obtained, it is possible to name the term $(I + A\Delta t)$ as Φ, given that this term represents a first order approximation of the state transition matrix reported in [7]. An alternative expression for equation 21 can be obtained if the STM is used directly to represent the system's dynamics.

Both representations are equivalent if the time step Δt is sufficiently small, but the STM form should be used in case the time step has to be increased. As previously mentioned in Section I, one of this work's objectives is the derivation of the continuous-time model, which motivates the selection of the formulation presented in equation 21 to describe the system dynamic's in the optimal control problem.

Then, the objective function must be also discretised. Assuming that the control actions $\boldsymbol{u}_j[k]$ are constant during the discretised time intervals, the objective function can be written as:

$$J = \sum_{j=1}^{j=N} \sum_{k=1}^{k=K-1} ||\boldsymbol{u}_j[k]||_1 \Delta t \tag{22}$$

The initial and final conditions are easily discretised, since they only involve the states at individual time instants:

$$\boldsymbol{\delta\alpha_j}[1] = \delta\alpha_{0,j} \tag{23}$$

$$\boldsymbol{\delta\alpha_j}[K] = \delta\alpha_{f,j} \tag{24}$$

The thrust level constraint is also easily transformed into discrete form:

$$||\boldsymbol{u}_j[k]|| \leq a_{max,j} \tag{25}$$

Finally, the safety distance constraint not only requires a discretisation but also a transformation into a suitable formulation for the convex optimal problem. The transformation performed here is based on the transformation formulated in [11]. The main idea behind this transformation is restricting the distance between the deputy j and a plane perpendicular to the relative position between satellites j and i. This means that the prohibited zone goes from being an sphere centred around the deputies to a polygonal volume centred around them, with each of their faces perpendicular to the relative position vectors between the deputies themselves. This idea is illustrated by Figs. 3a and 3b.

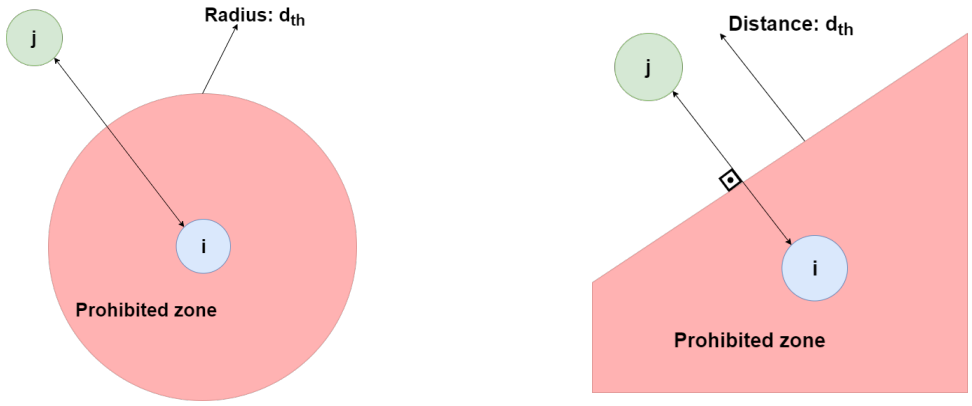

(a) Non-convex prohibited zone. **(b) Convex prohibited zone.**

Fig. 3 Graphical interpretation to the constraint transformation for safety distance. Inspired by similar figures in [11].

The main disadvantage related to this transformation is the fact that a reference or a previous relative position vector between the deputies is needed to compute all the prohibited zone faces, as explained at the end of this section. Assuming that a reference or a previous evolution of the ROEs is known, the safety distance constraint can be written as:

$$(L[k]\boldsymbol{\delta\bar{\alpha}_j}[k] - L[k]\boldsymbol{\delta\bar{\alpha}_i}[k])^T(L[k]\boldsymbol{\delta\alpha_j}[k] - L[k]\boldsymbol{\delta\alpha_i}[k]) \geq d_{th}||L[k]\boldsymbol{\delta\bar{\alpha}_j}[k] - L[k]\boldsymbol{\delta\bar{\alpha}_i}[k]||_2 \tag{26}$$

where $\boldsymbol{\delta\bar{\alpha}_i}$ and $\boldsymbol{\delta\bar{\alpha}_j}$ refer to the previous or the reference trajectory in the ROEs state space. The subindexes of the matrices L have been discarded, since they do not depend on the deputy. Taking this into account, the inequality's left-side term corresponds to the scalar product of the current relative vector between deputy i and deputy j and the previous or reference one. On the other side, the right-side of the inequality represents the modulus of the previous or reference relative vector multiplied by the minimum allowed inter-satellite distance. Since the scalar product can be decomposed as the multiplication of both modulus and the angle between both vectors, the terms corresponding to the reference or previous vector modulus cancel out from both sides, leaving the inequality as: the current relative vector between deputies i and j projection on the previous or reference direction must be bigger than or equal to the minimum allowed inter-satellite distance.

To solve this problem, all the variables of the optimisation problem must be collected into a single variable vector, and all the constraints and the objective function expressed as a direct function of this vector variable. The vector $\hat{\boldsymbol{x}}_j$ can be defined for each deputy j, including both the state variables and the control, as:

$$\hat{\boldsymbol{x}}_j = \left[\boldsymbol{\delta\alpha_{j,1}}\ ,\ \ \ldots\ ,\ \ \boldsymbol{\delta\alpha_{j,k}}\ ,\ \ \ldots\ ,\ \ \boldsymbol{\delta\alpha_{j,K}}\ ,\ \boldsymbol{u}_{j,1}\ ,\ \ \ldots\ ,\ \ \boldsymbol{u}_{j,k}\ ,\ldots\ ,\ \ \boldsymbol{u}_{j,K-1}\right]^T \tag{27}$$

In $\hat{\boldsymbol{x}}_j$, each $\delta\alpha_{j,k}$ corresponds to the ROEs of the j-th deputy at time instant t_k, and has therefore 6 elements. On the other hand, each $\boldsymbol{u}_{j,k}$ corresponds to the control action in RTN frame for the j-th deputy at time instant t_k, and has three elements. Consequently, the total length of $\hat{\boldsymbol{x}}_j$ is $M = 6K + 3(K-1)$. Putting together all the $\hat{\boldsymbol{x}}_j$ for all the deputies, the vector with all the optimisation variables is created, with a size of $(N \cdot M \times 1)$:

$$\hat{\boldsymbol{X}} = \left[\hat{\boldsymbol{x}}_1\ ;\ \ \ldots\ ;\ \hat{\boldsymbol{x}}_j\ ;\ \ \ldots\ ;\ \hat{\boldsymbol{x}}_N\right] \tag{28}$$

Once the total variable vector has been defined, the objective function and all the constrains can be expressed as a function of it. Starting from the system's dynamics, Eq. (21) for deputy j at time instant t_k can be written as:

$$\boldsymbol{\delta\alpha_{j,k+1}} = (I + A_k\Delta t)\boldsymbol{\delta\alpha_{j,k}} + \Delta t B_k \boldsymbol{u}_{j,k} \tag{29}$$

The matrices $A_{j,k}$ and $B_{j,k}$ do not depend on any parameter of the deputies, thus being equal for all of them. This means that the subscript $\cdot_j$ can be dropped, only depending on the time instant. It is possible to define a matrix $A_{sd,k}$ as

in Eq. (30), which recovers the necessary state vectors $\delta\alpha_{j,k+1}$, $\delta\alpha_{k,j}$ and $\boldsymbol{u}_{j,k}$ from the corresponding $\hat{\boldsymbol{x}}_j$ vector.

$$A_{sd,k} = \begin{bmatrix} \mathbf{0}_{6\times 6(k-1)} & -(I_6 + A_k\Delta t) & I_6 & \mathbf{0}_{6\times 3(2K-k-3)} & -B_k\Delta t & \mathbf{0}_{6\times 3(K-k-1)} \end{bmatrix} \tag{30}$$

These matrices $A_{sd,k}$ can be arranged in a bigger matrix $\hat{A}_{sd}$ to extract the necessary vectors from the total state vector $\hat{\boldsymbol{X}}$:

$$\hat{A}_{sd} = \begin{bmatrix} \dots & \dots & \dots \\ \mathbf{0}_{6\times M(j-1)} & A_{sd,k-1} & \mathbf{0}_{6\times M(N-j)} \\ \mathbf{0}_{6\times M(j-1)} & A_{sd,k} & \mathbf{0}_{6\times M(N-j)} \\ \mathbf{0}_{6\times M(j-1)} & A_{sd,k+1} & \mathbf{0}_{6\times M(N-j)} \\ \dots & \dots & \dots \end{bmatrix} \tag{31}$$

Where the index k goes from $k = 1$ to $k = K - 1$ for all $j = 1...N$. With this structure, the first $6(K-1)$ rows correspond to the necessary terms to obtain all the discretised dynamic equations for deputy 1, the second $6(K-1)$ correspond to the same but for deputy 2 and this is repeated until the last $6(K-1)$ correspond to all the terms necessary to obtain the discretised equations for deputy N. Consequently, the size of matrix $\hat{A}_{sd}$ is $(6(K-1)N \times M \cdot N)$, and the system's dynamics can be written as in Eq. (32).

$$\hat{A}_{sd}\hat{\boldsymbol{X}} = 0 \tag{32}$$

With a similar approach, also the objective function can be expressed as a function of the total state vector $\hat{\boldsymbol{X}}$. A set of matrices that extract all the control actions from the individual $\hat{\boldsymbol{x}}_j$ were constructed, which were then assembled to work with $\hat{\boldsymbol{X}}$. The matrix that extracts the control actions from the individual $\hat{\boldsymbol{x}}_j$ vectors is defined in equation 33:

$$H_j = \begin{bmatrix} \mathbf{0}_{3(K-1)\times 6K} & I_{3(K-1)} \end{bmatrix} \tag{33}$$

Once the matrix H_j is defined, the total assembly $\hat{H}$ can be defined as:

$$\hat{H} = \begin{bmatrix} \dots & \dots & \dots \\ \mathbf{0}_{3(K-1)\times M(j-1)} & H_j & \mathbf{0}_{3(K-1)\times M(N-j)} \\ \dots & \dots & \dots \end{bmatrix} \tag{34}$$

Where the index j goes from $j = 1$ to $j = N$. As a consequence, the objective function can be written as:

$$J = ||\hat{H}\hat{\boldsymbol{X}}\Delta t||_1 \tag{35}$$

Next, the initial and final conditions must be written as a function of the total variable vector $\hat{\boldsymbol{X}}$. To do so, the matrices A_{ic} and $A_{f,c}$ are defined as follows:

$$A_{ic} = \begin{bmatrix} I_6 & \mathbf{0}_{6\times M-6} \end{bmatrix}, \qquad A_{fc} = \begin{bmatrix} \mathbf{0}_{6\times 6K-6} & I_6 & \mathbf{0}_{6\times 3(K-1)} \end{bmatrix} \tag{36}$$

These matrices extract the first six ROEs of $\hat{\boldsymbol{x}}_j$ and the last six respectively, which correspond to the exact values that must be imposed as initial and final conditions. This process must done for all the deputies, so the matrix $\hat{A}_{ic}$ is assembled as in Eq. (37), while matrix $\hat{A}_{fc}$ has exactly the same distribution, changing A_{ic} for A_{fc}.

$$\hat{A}_{ic} = \begin{bmatrix} \dots & \dots & \dots \\ \mathbf{0}_{6\times M(j-1)} & A_{ic} & \mathbf{0}_{6\times M(N-j)} \\ \dots & \dots & \dots \end{bmatrix} \tag{37}$$

The initial and final conditions can be written as a function of $\hat{\boldsymbol{X}}$ as long as the vectors $\boldsymbol{\delta\alpha_{0,j}}$ and $\boldsymbol{\delta\alpha_{f,j}}$ are assembled as two column vectors $\boldsymbol{\delta\alpha_0} = \begin{bmatrix} \boldsymbol{\delta\alpha_{0,1}} & \dots & \boldsymbol{\delta\alpha_{0,N}} \end{bmatrix}^T$ and $\boldsymbol{\delta\alpha_f} = \begin{bmatrix} \boldsymbol{\delta\alpha_{f,1}} & \dots & \boldsymbol{\delta\alpha_{f,N}} \end{bmatrix}^T$.

$$\hat{A}_{ic}\hat{\boldsymbol{X}} = \boldsymbol{\delta\alpha_0} \tag{38}$$

$$\hat{A}_{fc}\hat{\boldsymbol{X}} = \boldsymbol{\delta\alpha_f} \tag{39}$$

The next constraint to be rearranged is the thrust level limitation. In this case, since the control is limited in both positive and negative values, the required matrix must take not only the control actions but also their negative values from the variables vector. The matrices $\tilde{A}_{th}$ and A_{th} are defined as:

$$\tilde{A}_{th} = \begin{bmatrix} \mathbf{0}_{3(K-1)\times 6K} & I_{3(K-1)} \end{bmatrix}, \qquad A_{th} = \begin{bmatrix} \tilde{A}_{th} \\ -\tilde{A}_{th} \end{bmatrix} \tag{40}$$

Where the matrix $\tilde{A}_{th}$ extracts the control actions from the individual variable vectors, and therefore the matrix A_{th} computes not only the control actions but also their negative counterparts. Again, these matrices can be arranged in a bigger matrix to take into account not the individual $\hat{\boldsymbol{x}}_j$ but the total one $\hat{\boldsymbol{X}}$, as in Eq. (41).

$$\hat{A}_{th} = \begin{bmatrix} \cdots & \cdots & \cdots \\ \mathbf{0}_{6(K-1)\times M(j-1)} & A_{th} & \mathbf{0}_{6(K-1)\times M(N-j)} \\ \cdots & \cdots & \cdots \end{bmatrix} \tag{41}$$

Thus, the thruster level limitation can be written as:

$$\hat{A}_{th}\hat{\boldsymbol{X}} \leq a_{max}B_{th} \tag{42}$$

Where the matrix B_{th} takes into account whether all the thrusters are limited to the same level or some of them have different limitations. An example of a different limitation is the case in which one of the directions has actually no control available, being in this case the maximum thrust possible 0. The matrices B_{th} corresponding to the case in which all thrusters have the same limitation and the one in which the radial direction cannot provide any thrust are included in Eq. (43):

$$B_{th} = \begin{cases} \mathbf{1}_{6N(K-1)\times 1} \\ \begin{bmatrix} 0 & 1 & 1 & 0 & 1 & 1 & \ldots & 0 & 1 & 1 \end{bmatrix}^T \end{cases} \tag{43}$$

Finally, the safety distance constraint was manipulated algebraically. First of all, the matrix $A_{CA}^{i,j}[k]$ has to be defined, which computes the relative position vector between deputies j and i at time instant t_k:

$$\begin{aligned} A_{CA}^{i,j}[k] = \big[\mathbf{0}_{3\times M(j-1)} \quad \mathbf{0}_{3\times 6(k-1)} \quad L_k \quad \mathbf{0}_{3\times 6(K-k)} \quad \mathbf{0}_{3\times 3(K-1)} \quad \cdots \\ \ldots \quad \mathbf{0}_{3\times M(i-j-1)} \quad \mathbf{0}_{3\times 6(k-1)} \quad -L_k \quad \mathbf{0}_{3\times 6(K-k)} \quad \mathbf{0}_{3\times 3(K-1)} \quad \mathbf{0}_{3\times M(N-i)}\big] \end{aligned} \tag{44}$$

In Eq. (44), the first zero matrix is used to enter the individual vector variable $\hat{\boldsymbol{x}}_j$. The second one is used to arrive to the ROEs of deputy j at time instant t_k. Then, the matrix L_k computes the relative cartesian position for the deputy j at time instant t_k, the third zero matrix is used to enter the part of the $\hat{\boldsymbol{x}}_j$ containing the control actions and the matrix $\mathbf{0}_{3\times 3(K-1)}$ is used to avoid that same part. Then the process is repeated but for deputy i, computing in this case the negative counterpart of the relative cartesian positions, so that they are subtracted from those belonging to deputy j and their relative position vector is obtained. The product $A_{CA}^{i,j}[k]\hat{\boldsymbol{X}}$ computes the relative position vector between deputies i and j:

$$A_{CA}^{i,j}[k]\hat{\boldsymbol{X}} = \begin{bmatrix} X_j(t_k) - X_i(t_k) \\ Y_j(t_k) - Y_i(t_k) \\ Z_j(t_k) - Z_i(t_k) \end{bmatrix} \tag{45}$$

Taking this into account, the projection of the current relative position vector between deputies j and i on the reference or previous relative vector can be computed as:

$$(L[k]\delta\bar{\alpha}_j[k] - L[k]\delta\bar{\alpha}_i[k])^T(L[k]\delta\alpha_j[k] - L[k]\delta\alpha_i[k]) = \bar{\boldsymbol{X}}^T(A_{CA}^{i,j})^T[k]A_{CA}^{i,j}[k]\hat{\boldsymbol{X}} \tag{46}$$

Where $\bar{\boldsymbol{X}}$ corresponds to a variable vector with the same structure as $\hat{\boldsymbol{X}}$ but related to the previous or reference solution. This projection must be computed once per each time instant and deputy combination, leaving a total computation number of $n_{rep} = \frac{N!}{2!(N-2)!}K$. This means that increasing the number of deputies affects the total computational time, which is related to the matrices' size. This, in turn, might lead to higher delays between the manoeuvre planning and the execution, and therefore, reducing the total performance. With this, the matrices $\bar{X}_M$ and $\hat{A}_{CA}$ can be built as in Eq. (47):

$$\bar{X}_M = \begin{bmatrix} \dots & \dots & \dots \\ \mathbf{0}_{1\times MN(gg-1)} & \bar{\boldsymbol{X}}^T & \mathbf{0}_{1\times MN(n_{rep}-gg)} \\ \dots & \dots & \dots \end{bmatrix}, \qquad \hat{A}_{CA} = \begin{bmatrix} \dots \\ (A_{CA}^{i,j}[k-1])^T A_{CA}^{i,j}[k-1] \\ (A_{CA}^{i,j}[k])^T A_{CA}^{i,j}[k] \\ (A_{CA}^{i,j}[k+1])^T A_{CA}^{i,j}[k+1] \\ \dots \end{bmatrix} \tag{47}$$

Matrix $\bar{X}_M$ is built in such a way that each row contains the full vector $\bar{\boldsymbol{X}}$ transposed and placed in different columns inside the matrix, so that the product computed is the correct one. The index gg in Eq. (47) goes from $gg = 1$ to $gg = n_{rep}$, meaning that $\bar{X}_M$ is a $(n_{rep} \times M \cdot N \cdot n_{rep})$ matrix. On the other hand, matrix $\hat{A}_{CA}$ simply contains the matrix products necessary to compute the projection as in Eq. (46). The last remark worth mentioning is the fact that these matrices also allow computing the modulus of the previous or reference relative vectors, which is necessary for the safety distance constraint. This is shown in Eq. (48), where the final discretised convex safety distance constraint is written.

$$\bar{X}_M\hat{A}_{CA}\hat{\boldsymbol{X}} \geq d_{th}\sqrt{\bar{X}_M\hat{A}_{CA}\bar{\boldsymbol{X}}} \tag{48}$$

Where the product $\bar{X}_M\hat{A}_{CA}\bar{\boldsymbol{X}}$ computes the squared modulus of the reference or previous relative position vector at

each time instant and for all the deputy combinations. Thus, taking the square root of the individual components of this column vector provides the necessary modulus at each time instant.

Finally, all the equations involved in the problem have been discretised and transformed in terms of $\bar{\boldsymbol{X}}$. The convex optimal problem is written in Eq. (49) as a summary.

$$\begin{aligned} &\text{Minimise:} && J = ||\hat{H}\hat{\boldsymbol{X}}\Delta t||_1 \\ &\text{subject to:} && \hat{A}_{sd}\hat{\boldsymbol{X}} = 0 \\ & && \hat{A}_{ic}\hat{\boldsymbol{X}} = \boldsymbol{\delta\alpha_0} \\ & && \hat{A}_{fc}\hat{\boldsymbol{X}} = \boldsymbol{\delta\alpha_f} \\ & && \hat{A}_{th}\hat{\boldsymbol{X}} \leq a_{max}B_{th} \\ & && \bar{X}_M\hat{A}_{CA}\hat{\boldsymbol{X}} \geq d_{th}\sqrt{\bar{X}_M\hat{A}_{CA}\bar{\boldsymbol{X}}} \end{aligned} \tag{49}$$

An important consideration is related to the reference/previous state vector. This is where the SCP formulation comes into play. Following the approach in [11], the problem is solved in a recursive manner, updating the reference solution $\bar{\boldsymbol{X}}$ each iteration with the previous solution $\hat{\boldsymbol{X}}$. This iteration is repeated until the new solution $\hat{\boldsymbol{X}}$ and the previous one $\bar{\boldsymbol{X}}$ are sufficiently close to each other, measured by the infinite norm of their difference $||\hat{\boldsymbol{X}} - \bar{\boldsymbol{X}}||_\infty$. The only case where this is not applicable is the first iteration, in which the problem must be solved without the safety distance constraint to obtain the first reference solution. This resolution of the first iteration without the distance constraint allows obtaining more consistent solutions for this problem, that do not depend so heavily in the initial estimated trajectory provided to the solver [12].

Solving the convex optimal control problem presented in Eq. (49) allows obtaining the necessary control actions that each deputy has to apply at each time instant t_k and their corresponding ROEs during the manoeuvre. This means that this formulation is a centralised one, as the problem is solved for all the deputies involved in the manoeuvre at the same time. This implies that it suffers of bad scaling with the number of deputies, because the number of inter-satellite distance constraints that have to be checked increases quadratically with the number of deputies. In order to improve the resolution time required to solve the problem with an increasing number of deputies, the formulation could be modified in such a way that each satellite computes their own required control actions and only takes into account those deputies that might pose a collision threat, as proposed in [11].

IV. Results

In Section III, all the theoretical and mathematical formulations for the control algorithm were presented and developed. This section presents the results of the numerical simulations performed to test this algorithm, and provides a small description of the formation geometries considered to test the control algorithms. Then, the results corresponding

to the open-loop manoeuvre planning algorithm are introduced and described, including an explanation of how these numerical simulations were performed.

There are several different open-source software that solve convex optimal problems. SeDuMi is the one considered in this article, developed by F. Sturm [35] and it is included by default among the available solvers for the CVX software, which is an open-source $MATLAB^{©}$-based modelling system for convex optimisation [36, 37], developed by M. Grant and S. Boyd. The reason why this particular solver is considered instead of the other options available for CVX is because it allows obtaining better results in terms of convergence rate and time for most of the cases considered.

Before presenting the results for the first manoeuvre, it is necessary to point out that the formulation reported in Eq. (49) suffers from numerical bad-conditioning, because of the different equations' orders of magnitude. In particular, the safety distance constraint is several orders of magnitude higher than the other equations, mainly due to the presence of the chief's semi-major axis squared inside $\hat{A}_{CA}$. Two possible ways to handle this problem were identified. First, the order of magnitude of this constraint can be artificially reduced, thanks to a multiplicative gain. A second approach consists in reformulating the whole problem in a non-dimensional way.

The first approach is considered in this paper, with a gain of $1 \cdot 10^{-9}$ on both sides of the inequality in Eq. (48).

A. Test cases description

This section includes the descriptions of the two test cases considered to evaluate the algorithm's performances.

1. Test case 1: formation flying for remote sensing (3 satellites)

The first test case scenario is based on the Formation Flying L-Band Aperture Synthesis mission concept under study by ESA, Airbus and Politecnico di Milano, consisting of a group of three L-band satellites [38], which aims at increasing the spatial resolution of synthetic aperture instruments. The reference mean orbit for this formation is a sun-synchronous orbit with the following characteristics [20]: mean altitude of 775 km and mean inclination of 98.5 º. As described in previous works [20], the formation is shaped as a 13 m side equilateral triangle, with the satellites placed at the vertex. The chief virtual satellite corresponds to the triangle's centre. This triangle lies on a plane perpendicular to the position vector and must be fixed, which means that control actions are required to counteract the natural dynamics of the formation, which would tend to deform this triangle.

As described in [20], each spacecraft has a total weight of about 1600 kg, meaning that these deputies are not in the small sized category previously mentioned in Section I. Their radius is 3.5 m, which means that a minimum inter-satellite distance constraint of at least $d_{th} = 10$ m should be imposed to ensure no collision occurs. They are equipped with low-thrust propulsion technology in order to perform continuous orbit control. The baseline is the engine QinetiQ T5, which can provide a maximum thrust of 25 mN. Taking into account that the constraint inside the optimal control problems is formulated with the acceleration as the control variable, this maximum thrust has to be transformed into a maximum acceleration, which corresponds to $a_{max} = 1.5625 \cdot 10^{-5}$ m/s^2. Furthermore, in this analysis the

spacecraft are assumed to provide thrust only in normal and transversal directions. This limitation comes from the design itself, as the weight reduction was paramount and no thruster in the radial direction was included. It must be considered inside the optimal control problem with a suitable B_{th} matrix, as in equation Eq. (42). This formation was selected mainly because it is a tight formation, which poses a bigger challenge for control algorithms, due to the close distance between the desired relative cartesian position and the prohibited zones due to collision risks.

2. Test case 2: formation flying for space advertisement (5 satellites)

The second test case considered is based on the analysis done in [39], where the preliminary mission analysis and conceptual design of a reflective balloon mission is performed, studying whether it would be possible to launch a satellite that could be visible with naked eyes from several different cities across the world. Such satellite could be used in a formation to perform activities that required direct visual contact from the ground, like advertisement. The chief's orbital elements are reported in Table 3, as in Table 5.1 of [39].

Table 3 Chief's orbital elements for the balloon mission formation [39].

a [m]	**e** [-]	**i** [º]	Ω [º]	ω [º]	M_0 [º]
7266500	0.001	99	285	0	90

In this case, the formation's chief virtual satellite corresponds to the formation's geometrical centre. Its orbital elements correspond to those of a repeated groundtrack and sun-synchronous orbit. The groundtrack repetition was a requirement to re-visit the points of interest on Earth's surface with a high frequency [39]. The sun-synchronicity, instead, was required to ensure a correct power supply, but most importantly to ensure that the lighting conditions needed to see the satellites with the naked eye from the ground were always achieved [39].

The mission consists of five deputies, which could have two configurations. The first one is a linear configuration in the tangential direction with a 25 m inter-satellite separation. The second one is a circular configuration on the tangential-normal plane with a 20 m radius and with the deputies spread along the circumference with an equal angular separation. This results in a pentagonal configuration. The corresponding ROEs and relative cartesian positions are further reported in Section IV.C, where the results for the transition manoeuvre are described.

The numerical values for the thrust limitation and inter-satellite constraints must be changed to match the specifications included in [39]. Regarding the thrust limitation, the total preliminary mass budget reported for this type of spacecraft is around 100 kg [39]. Assuming that they are equipped with low-thrust electrical propulsion technology with a maximum thrust of 25 mN, the new thrust limitation value becomes $a_{max} = 2.5 \cdot 10^{-4}$ m/s^2. The balloon used in these spacecraft to reflect light and to allow them to be seen from ground must always point in the radial direction. For this reason, these spacecraft are considered unable to provide thrust in the radial direction, which is completely occupied by the balloon.

Moreover, the inter-satellite distance constraint should consider the balloon dimensions reported in [39]. The selected balloon radius in this reference is around 4.4 m, which can be rounded up to 5. A collision between spacecraft

will occur if both centres are closer than 10 meters. To ensure a safety margin, the minimum allowable inter-satellite distance for this formation is set to $d_{th} = 20$ m.

B. Test case 1: Payload calibration

The first manoeuvre considered is the so-called payload calibration manoeuvre considered in the FFLAS formation design. In this manoeuvre, the objective is to switch the positions of the two deputies placed at the top of the triangle (2 and 3) so that their payload can be calibrated [12]. This manoeuvre has to be performed regularly during the mission period, so achieving a predefined optimal manoeuvre from the fuel consumption point of view is crucial. The chief's absolute orbital elements, the deputies' initial ROEs and their initial relative cartesian positions considered in this simulation are included in Tables 4 to 6.

Table 4 Chief's orbital elements

a [m]	**e** [-]	**i** [º]	Ω [º]	ω [º]	M_0 [º]
7153140	0.001	98.5	34	0	90

Table 5 Initial ROEs for the payload calibration manoeuvre.

Dep.	δa [-]	$\delta\lambda$ [-]	δe_x [-]	δe_y [-]	δi_x [-]	δi_y [-]
1	0	0	0	0	$-5.2483\cdot10^{-7}$	0
2	0	$9.0869\cdot10^{-7}$	0	0	$1.0491\cdot10^{-6}$	0
3	0	$-9.0869\cdot10^{-7}$	0	0	$1.0491\cdot10^{-6}$	0

Table 6 Initial and final relative cartesian positions for the payload calibration manoeuvre.

	Initial			**Final**		
	X [m]	Y [m]	Z [m]	X [m]	Y [m]	Z [m]
Dep. 1	0	0	-3.7542	0	0	-3.7542
Dep. 2	0	6.5	7.5042	0	-6.5	7.5042
Dep. 3	0	-6.5	7.5042	0	6.5	7.5042

Although the chief's orbit is defined as circular in Section IV.A.1, a small eccentricity is considered in this simulation to account for a more realistic scenario, in which a completely circular orbit cannot be achieved. It is also worth mentioning that the right ascension of the ascending node Ω was selected as a generic value, since it does not influence the manoeuvre at all.

This manoeuvre planning problem is solved using SeDuMi and the desired time to complete the reconfiguration is set to 3/4 of the chief's orbital period, considering $d_{th} = 10$ m as the minimum inter-satellite distance constraint. The discretisation step considered for this manoeuvre is $\Delta t = 25$ s. The results obtained from the resolution of the problem described by Eq. (49) with the previously shown initial conditions, the desired reconfiguration and $d_{th} = 10$ m are

shown in Fig. 4.

In Fig. 4a, each deputy's initial position is marked with a triangle in their corresponding colours. The optimal solution for the payload calibration manoeuvre is a symmetric trajectory with respect to the $X = 0$ plane. As shown in Figs. 4b and 4d, even though deputy 1 is not commanded to change positions, it has to move during the manoeuvre. This is due to the minimum inter-satellite distance constraint, which would be violated as seen in Fig. 4c if the deputy 1 would not move. The limitation imposed to the deputies' accelerations is also respected, as seen in Fig. 4b. The radial component remains equal to zero for the three deputies during the whole manoeuvre and the other two components are below the $a_{max} = 1.5625 \cdot 10^{-5}$ m/s^2 limit, both in the positive and in the negative direction.

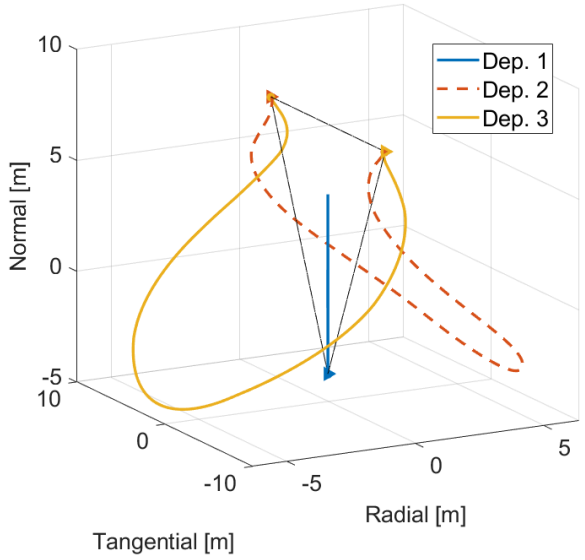

(a) Deputies' trajectories in 3D space.

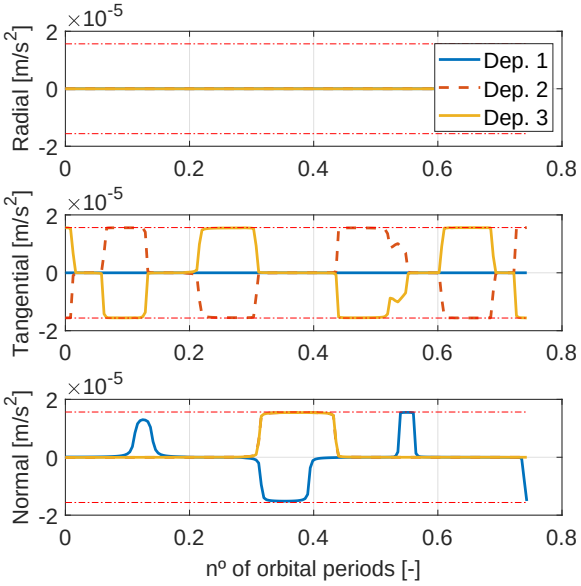

(b) Required accelerations.

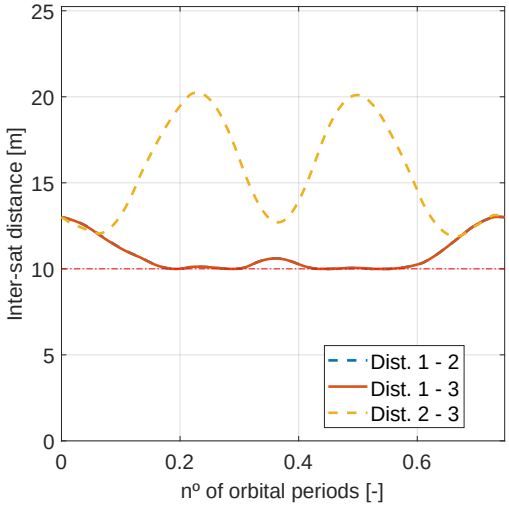

(c) Inter-satellite distance along the manoeuvre.

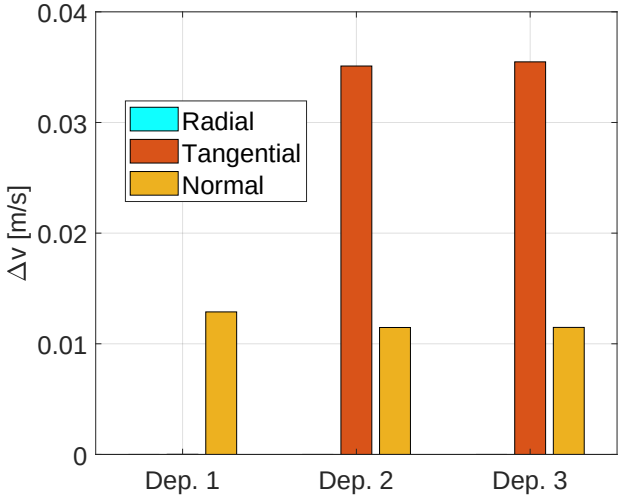

(d) Total ΔV budget required by each deputy.

Fig. 4 Open-loop manoeuvre planning results for payload calibration manoeuvre with $d_{th} = 10$ m.

On the other hand, the total ΔV budget for all three deputies needed to perform this manoeuvre is 0.1045 m/s. One of the apparent advantages of working with ROEs is that they seem to increase the optimisation's efficiency, thanks to the better geometrical insight that the ROEs give to the optimisers, which in turn, can obtain better solutions. However, this should be proven mathematically in future works. Finally, in the acceleration temporal evolution's normal component in Fig. 4b, those associated to deputies 2 and 3 are so similar that are almost indistinguishable. The same happens for the inter-satellite distance between deputies 1 - 2 and 1 - 3 in Fig. 4c.

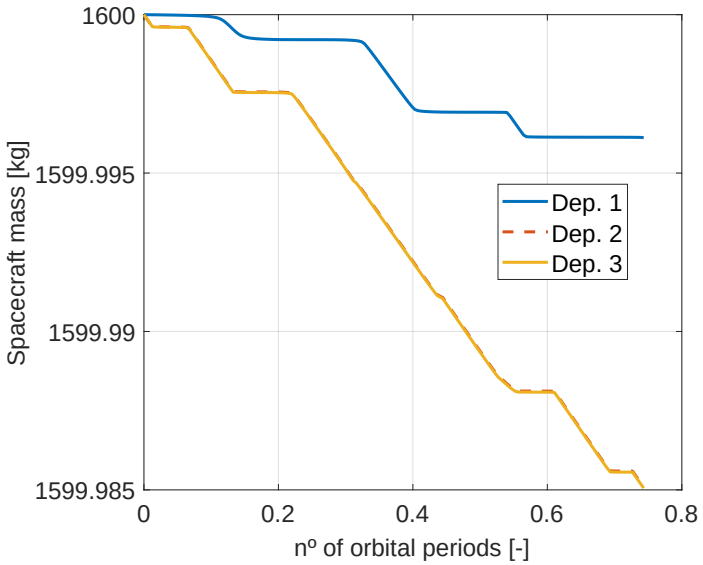

Fig. 5 Mass evolution during the payload calibration manoeuvre for each satellite.

Another interesting result is the mass variation of each of the deputies during the manoeuvre, as shown in 5. Comparing this figure to 4b, it is apparent how the mass decreases each time the thrusters are fired, but also how the total mass variation during the whole manoeuvre is minute. This is in line with the high total impulse associated with the electric propulsion considered and the low levels of acceleration required during the manoeuvre.

This solution was obtained in 31 s on a Windows computer with Intel(R) Core(TM) i7-8750H CPU @ 2.20GHz at 2.20 GHz and 16.0 GB of RAM, requiring 5 iterations to fully converge, counting the initial one in which the safety distance constraint was not taken into account. This means that each iteration, including the computation of $\bar{X}_M$, took around 6 seconds.

C. Test case 2: Line to Circle manoeuvre

The second manoeuvre included in this article is the transition from the linear configuration to the circular one for the 5 deputy formation described in Section IV.A.2. The ROEs' values for the initial formation configuration and the relative cartesian coordinates for the initial and final configurations are reported in Tables 7 and 8. Given that the initial configuration is along the tangential direction, only the relative longitudes have been reported in Table 7, as the other ROEs are all zero.

Table 7 Initial ROEs for the Line to Circle manoeuvre.

Dep.	**1**	**2**	**3**	**4**	**5**
$\delta\lambda \cdot 10^6$ [-]	0	3.4404	6.8809	-3.4404	-6.8809

Table 8 Initial and final relative cartesian positions for the Line to Circle manoeuvre.

	Initial			**Final**		
	X [m]	Y [m]	Z [m]	X [m]	Y [m]	Z [m]
Dep. 1	0	0	0	0	0	20
Dep. 2	0	25	0	0	11.7557	-16.1803
Dep. 3	0	50	0	0	19.0211	6.1803
Dep. 4	0	-25	0	0	-11.7557	-16.1803
Dep. 5	0	-50	0	0	-19.0211	6.1803

The selected reconfiguration time is left as $3/4$ of the chief's orbital period, with a discretisation step of $\Delta t = 25$ s. The results obtained for this manoeuvre with SeDuMi are reported in Fig. 6, where a view change with respect to the previous case was done to ease the visualisation of all the trajectories. There are several lines overlapped in Fig. 6c, due to the formation and manoeuvre's anti-symmetry. This property can also be observed in Figs. 6b and 6d, where deputies 2 - 4 and 3 5 have the exact same ΔV budget and an anti-symmetric control action temporal evolution.

The fact that the thrust limitation is almost never reached during the manoeuvre, as seen in Fig. 6b, suggests that this reconfiguration could be performed with a shorter manoeuvre or with a less powerful engine. This problem's scalability issue with the number of deputies can be observed in this case. With 5 deputies and a inter-satellite distance constraint of $d_{th} = 20$ m the total required time to obtain a solution was 664 s and a total number of 8 iterations to converge on the same Windows computer described in Section IV.B. This means that each iteration, including the $\bar{X}_M$ matrix computation, takes around 83 s, more than ten times the previous case. This is due to the higher number of deputies involved in the manoeuvre. The spacecraft design described in [39] includes the aforementioned reflective balloon which, due to its big surface, would be affected by the solar radiation pressure, to the point where it could reach orders of magnitude similar to those of the J_2 perturbation. Because the solar radiation pressure has not been taken into account in this article, applying this manoeuvre for a formation composed by such spacecraft might lead to slight discrepancies between the desired final positions and the final ones. Nonetheless, the mission described in [39] and the manoeuvre here presented could be applied to a formation of small self-illuminated satellites, which achieve the required level of brightness through a set of LEDs instead of direct reflection [40].

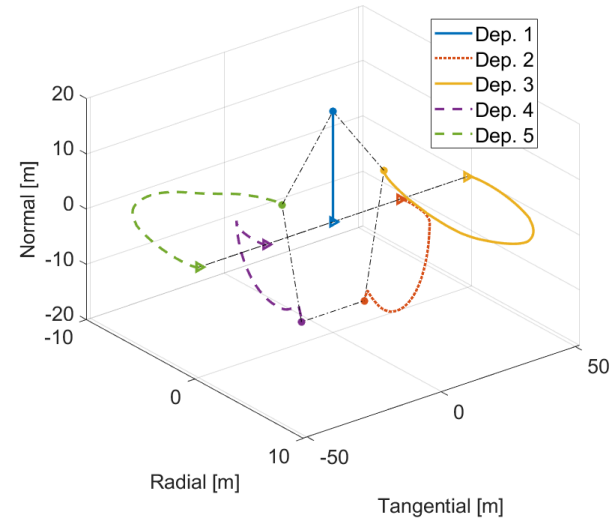

(a) Deputies' trajectories in 3D space.

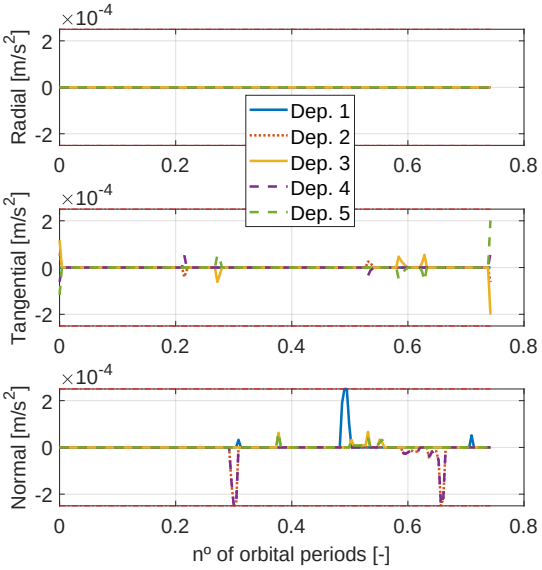

(b) Required accelerations.

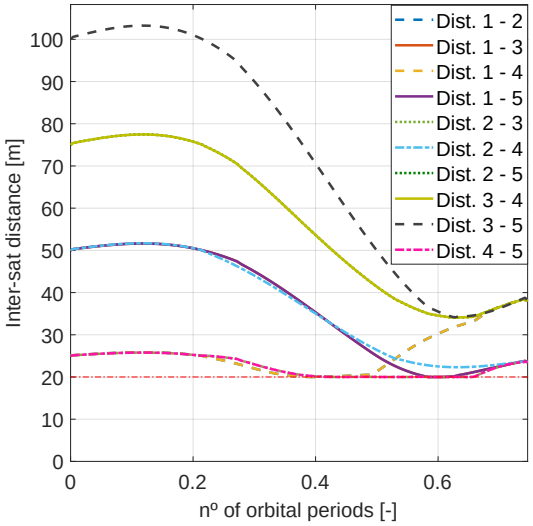

(c) Inter-satellite distance along the manoeuvre.

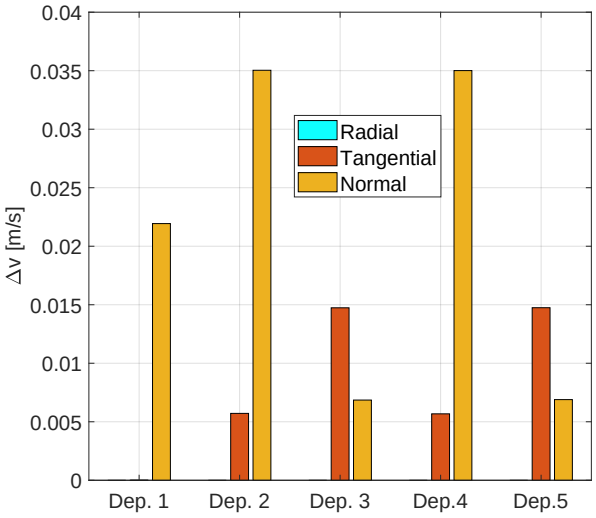

(d) Total ΔV budget required by each deputy.

Fig. 6 Open-loop manoeuvre planning results for Line to Circle manoeuvre with $d_{th} = 20$ m.

V. Conclusions

This article presents a new formation flying control problem based on the ROEs as state variables, and implements an open-loop manoeuvre planning algorithm, which expands the current catalogue of continuous-time and ROEs-based control algorithms. The ROEs' dynamics under the effects of Earth's gravity potential are expressed with a new continuous-time model, which was obtained thanks to the state transition matrix presented in [7]. Even though in this article only the Earth's oblateness effect was considered, this formulation could be generalised to J_n zonal harmonics.

Considering only the J_2 effect, the chief's semi-major axis remained unchanged because the zonal harmonics do not have any influence on it and therefore could be considered as a constant in the problem's formulation. To generalise

even more the problem formulation and include orbital perturbations affecting the semi-major axis of the orbit, such as the atmospheric drag, the equations would have to be revised to account for this semi-major axis change along time.

Working with the ROEs as state variables has several advantages. It allows obtaining fuel-efficient manoeuvres, due to the good geometrical insight provided by the ROEs. Whether this improvement in fuel consumption is related to this should be proven mathematically in future works. ROEs also allow obtaining directly information about the relative orbit geometry. Finally, ROEs' definition is not limited by the close proximity or chief's circular orbit assumptions that other formulations need.

The formulation presented in this article for the optimal control problem suffers from two issues: the first one is numerical bad-conditioning due to the very wide range of orders of magnitude involved in the equations. This is solved by artificially decreasing the distance constraint's order of magnitude, but a second approach from the numerical point of view would be to formulate the problem in a non-dimensional way. On the other hand, this formulation suffers from bad scaling with the number of deputies, as the number of inter-satellite distance constraints that have to be checked increases quadratically with the number of deputies. As already mentioned, a way of tackling this problem could be the formulation of a decentralised problem, in such a way that each satellite computes its control actions and only takes into account those deputies that might pose a collision threat, as proposed in [11].

The developed control algorithm is an open-loop manoeuvre planning, which, given an initial condition, a desired final condition and a manoeuvre duration, provides the required control actions along with the manoeuvre that minimises the fuel consumption and the associated ROEs. This algorithm has proven to correctly determine the accelerations required to perform several different manoeuvres, such as a triangular reconfiguration or a linear to circular transition. Both of these manoeuvres could be solved by the control algorithm because it is formulated for a generic number of deputies. One way to improve the current precision of the algorithm could be to increase the precision of the dynamic model discretisation, which right now is performed taking the first term of the $e^{A\Delta t}$ expression. The implications of taking more terms or even a completely different method for discretising the dynamics could be an interesting topic for a future work.

The fact that a continuous-time model was obtained from a discrete formulation of the dynamics to be then discretised again could seem like a roundabout way to get to the initial condition: a discrete model of the relative dynamics. However, the derivation of this continuous-time model is one of the objectives of this work, as this continuous-time formulation can be used to obtain non-linear controllers, such as those based on Lyapunov functions. The reason why a discrete-time based controller is presented in this work was not only to show the versatility of of this model, but also because the results obtained with this formulation were more satisfactory than those obtained with different continuous-time based controllers, which could not guarantee convergence for all the test scenarios, or in the best case where convergence was achieved, including the safety distance constraint in the problem proved to be challenging.

VI. Acknowledgments

The work presented in this paper was funded by the European Union's Horizon 2020 research and innovation program (grant agreement No. 679086 COMPASS).

References

[1] Martín-Neira, M., Suess, M., Karafolas, N., Piironen, P., Deborgies, F., Catalán, A., Vilaseca, R., Montero, J., Outumuro, D., Corbella, I., Durán, I., Duffo, N., Materni, R., Mengual, T., Angel, M., Olea, A., Solana, A., Closa, J., Zurita, A., Ramírez, J. I., Oliva, R., Onrubia, R., Camps, A., Querol, J., and Photonics, D. A. S., "Technology Developments for an Advanced L-Band Radiometer Mission," *IGARSS 2020-2020 IEEE International Geoscience and Remote Sensing Symposium*, 2020, pp. 6507–6510. https://doi.org/10.1109/IGARSS39084.2020.9324378.

[2] Tapley, B. D., Bettadpur, S., Watkins, M., and Reigber, C., "The gravity recovery and climate experiment: Mission overview and early results," *Geophysical Research Letters*, Vol. 31, No. 9, 2004, pp. 1–4. https://doi.org/10.1029/2004GL019920.

[3] Moreira, A., Krieger, G., Fiedler, H., Hajnsek, I., Werner, M., Zink, M., and Younis, M., "TanDEM-X: A satellite formation for high resolution radar interferometry," *AIAA 57th International Astronautical Congress, IAC 2006*, Vol. 3, No. 11, 2006, pp. 2075–2082. https://doi.org/10.2514/6.iac-06-b1.3.05.

[4] Verhoeven, C. J., Bentum, M. J., Monna, G. L., Rotteveel, J., and Guo, J., "On the origin of satellite swarms," *Acta Astronautica*, Vol. 68, No. 7-8, 2011, pp. 1392–1395. https://doi.org/10.1016/j.actaastro.2010.10.002.

[5] Martin, S., "Modern Small Satellites - Changing the Economics of Space," *Proceedings of the IEEE*, Vol. 106, 2018, pp. 343–361. https://doi.org/10.1109/JPROC.2018.2806218.

[6] Koenig, A. W., and D'Amico, S., "Robust and safe N-spacecraft swarming in perturbed near-circular orbits," *Journal of Guidance, Control, and Dynamics*, Vol. 41, No. 8, 2018, pp. 1643–1662. https://doi.org/10.2514/1.G003249.

[7] Gaias, G., Colombo, C., and Lara, M., "Analytical framework for precise relative motion in low earth orbits," *Journal of Guidance, Control, and Dynamics*, Vol. 43, No. 5, 2020, pp. 915–927. https://doi.org/10.2514/1.G004716.

[8] Starin, S. R., Yedavalli, R. K., and Sparks, A. G., "Design of a LQR controller of reduced inputs for multiple spacecraft formation flying," *Proceedings of the American Control Conference*, Vol. 2, 2001, pp. 1327–1332. https://doi.org/10.1109/ACC.2001.945908.

[9] Hadaegh, F. Y., Ghavimi, A. R., Gurkirpal, S., and Quadrelli, M., "A Centralized Optimal Controller for Formation Flying Spacecraft," *International Conference on Robotic Intelligence Technology*, Bangkok, Thailand, 2000, pp. 1–6. URL http://hdl.handle.net/2014/16143.

[10] Breger, L., Inalhan, G., Tillerson, M., and How, J. P., "Cooperative Spacecraft Formation Flying: Model Predictive Control with Open-and Closed-Loop Robustness," *Modern Astrodynamics*, Vol. 1, Elsevier UK, 2006, Chap. 8, elsevier a ed., pp. 237–277. https://doi.org/10.1016/S1874-9305(07)80010-0.

[11] Morgan, D., Chung, S. J., and Hadaegh, F. Y., "Model predictive control of swarms of spacecraft using sequential convex programming," *Journal of Guidance, Control, and Dynamics*, Vol. 37, No. 6, 2014, pp. 1725–1740. https://doi.org/10.2514/1.G000218.

[12] Scala, F., Gaias, G., Colombo, C., and Martín-Neira, M., "Design of optimal low-thrust manoeuvres for remote sensing multi-satellite formation flying in low Earth orbit," *Advances in Space Research*, Vol. 68, No. 11, 2021, pp. 4359–4378. https://doi.org/https://doi.org/10.1016/j.asr.2021.09.030.

[13] Tang, G. J., Luo, Y. Z., and Li, H. Y., "Optimal robust linearized impulsive rendezvous," *Aerospace Science and Technology*, Vol. 11, No. 7-8, 2007, pp. 563–569. https://doi.org/10.1016/j.ast.2007.04.001.

[14] Bennett, T., Schaub, H., and Roscoe, C. W., "Faster-than-natural spacecraft circumnavigation via way points," *Acta Astronautica*, Vol. 123, 2016, pp. 376–386. https://doi.org/10.1016/j.actaastro.2016.01.025.

[15] Montenbruck, O., Kirschner, M., D'Amico, S., and Bettadpur, S., "E/I-vector separation for safe switching of the GRACE formation," *Aerospace Science and Technology*, Vol. 10, No. 7, 2006, pp. 628–635. https://doi.org/10.1016/j.ast.2006.04.001.

[16] Montenbruck, O., Kahle, R., D'amico, S., and Ardaens, J. S., "Navigation and control of the TanDEM-X formation," *Journal of the Astronautical Sciences*, Vol. 56, No. 3, 2008, pp. 341–357. https://doi.org/10.1007/bf03256557.

[17] D'Amico, S., and Montenbruck, O., "Proximity operations of formation-flying spacecraft using an eccentricity/inclination vector separation," *Journal of Guidance, Control, and Dynamics*, Vol. 29, No. 3, 2006, pp. 554–563. https://doi.org/10.2514/1.15114.

[18] D'Amico, S., Ardaens, J. S., and Larsson, R., "Spaceborne autonomous formation-flying experiment on the PRISMA mission," *Journal of Guidance, Control, and Dynamics*, Vol. 35, No. 3, 2012, pp. 834–850. https://doi.org/10.2514/1.55638.

[19] Sutton, G. P., "Electric propulsion," *Rocket Propulsion Elements*, Wiley-Interscience, 2001, Chap. 19, seventh ed., pp. 660–661.

[20] Scala, F., Gaias, G., and Martin-neira, M., "Formation Flying L-band Aperture Synthesis: design challenges and innovative formation architecture concept," *Proceeding of the International Astronautical Congress - The CyberSpace Edition*, 2020, pp. 1–10. ISSN 00741795.

[21] Gaias, G. V., Lavagna, M. R., Golikov, A. R., and Ovchinnikov, M. Y., "Formation flying: Relative orbits' modelling and control through Eulerian orbital elements," *Advances in the Astronautical Sciences*, Vol. 134, No. January, 2009, pp. 1271–1283.

[22] Bennett, T., and Schaub, H., "Continuous-time modeling and control using nonsingular linearized relative-orbit elements," *Journal of Guidance, Control, and Dynamics*, Vol. 39, No. 12, 2016, pp. 2605–2614. https://doi.org/10.2514/1.G000366.

[23] D'Amico, S., "Relative Orbital Elements as Integration Constants of Hill's Equations," *Space Flight Technology, German Space Operations Center*, Vol. -, No. 1, 2005, pp. 3–12.

[24] Di Mauro, G., Bevilacqua, R., Spiller, D., Sullivan, J., and D'Amico, S., "Continuous maneuvers for spacecraft formation flying reconfiguration using relative orbit elements," *Acta Astronautica*, Vol. 153, No. March, 2018, pp. 311–326. https://doi.org/10.1016/j.actaastro.2018.01.043.

[25] Clemente, M. P., Battipede, M., and Ahn, J., *Optimal Control of Low-Thrust Satellite Formation-Flying Reconfiguration using a LQR*, Politecnico di Torino, 2020. (MSc Thesis).

[26] Steindorf, L. M., D'Amico, S., Scharnagl, J., Kempf, F., and Schilling, K., "Constrained low-thrust satellite formation-flying using relative orbit elements," *27th AAS/AIAA Space Flight Mechanics Meeting*, San Antonio, 2017, pp. 3563–3583.

[27] Schaub, H., Vadali, S. R., Junkins, J. L., and Alfriend, K. T., "Spacecraft formation flying control using mean orbital elements," *The Journal of the Astronautical Sciences*, Vol. 48, No. 1, 2000, pp. 69–87.

[28] Koenig, A. W., Guffanti, T., and D'Amico, S., "New state transition matrices for spacecraft relative motion in perturbed orbits," *Journal of Guidance, Control, and Dynamics*, Vol. 40, No. 7, 2017, pp. 1749–1768. https://doi.org/10.2514/1.G002409.

[29] NASA, "GMAT, General Mission Analysis Tool, Software Package, Version R2020a," , 2020.

[30] Brouwer, D., "Solution of the problem of artificial satellite theory without drag," *The Astronomical Journal*, Vol. 64, No. 1274, 1959.

[31] Gaias, G., and Lovera, M., "Proximity Operations Trajectory Design in the Relative Orbital Elements ' Perspective," *AerospaceEurope Conference*, Bordeaux, France, 2020, pp. 1–9.

[32] Boyd, S., and Vandenberghe, L., *Convex Optimization Problems*, Cambridge University Press, 2017. https://doi.org/10.1201/9781315366920-5.

[33] Sabatini, M., and Palmerini, G. B., "Linearized formation-flying dynamics in a perturbed orbital environment," *IEEE Aerospace Conference Proceedings*, 2008, pp. 1–13. https://doi.org/10.1109/AERO.2008.4526271.

[34] Hofmann, C., and Topputo, F., "Rapid Low-Thrust Trajectory Optimization in Deep Space Based on Convex Programming," *Journal of Guidance, Control, and Dynamics*, 2021, pp. 1–10. https://doi.org/10.2514/1.g005839.

[35] Sturm, J. F., "Using SeDuMi 1.02, a MATLAB toolbox for optimization over symmetric cones," *Optimization Methods and Software*, Vol. 11, No. 1, 1999, pp. 625–653. https://doi.org/10.1080/10556789908805766.

[36] Grant, M., and Boyd, S., "Graph implementations for nonsmooth convex programs," *Recent Advances in Learning and Control*, edited by V. Blondel, S. Boyd, and H. Kimura, Lecture Notes in Control and Information Sciences, Springer-Verlag Limited, 2008, pp. 95–110.

[37] Grant, M., and Boyd, S., "CVX: Matlab Software for Disciplined Convex Programming, version 2.1," , 2014.

[38] Mecklenburg, S., Drusch, M., Kerr, Y. H., Font, J., Martin-Neira, M., Delwart, S., Buenadicha, G., Reul, N., Daganzo-Eusebio, E., Oliva, R., and Crapolicchio, R., "ESA's soil moisture and ocean salinity mission: Mission performance and operations," *IEEE Transactions on Geoscience and Remote Sensing*, Vol. 50, No. 5 PART 1, 2012, pp. 1354–1366. https://doi.org/10.1109/TGRS.2012.2187666.

[39] Roccioletti, M. P., and Colombo, C., *Mission analysis and concept design for a reflective balloon mission*, Politecnico di Milano, 2018. (MSc Thesis).

[40] Santoni, F., Seitzer, P., Cardona, T., Locatelli, G., Marmo, N., Masillo, S., Morfei, D., and Piergentili, F., "Optical tracking and orbit determination performance of self-illuminated small spacecraft: LEDSAT (LED-based SATellite)," *Advances in Space Research*, Vol. 62, No. 12, 2018, pp. 3318–3334. https://doi.org/10.1016/j.asr.2018.08.018.